Plasma Sources Science and Technology

PAPER

Comparison of electron heating and energy loss mechanisms in an RF plasma jet operated in argon and helium

To cite this article: J Golda *et al* 2020 *Plasma Sources Sci. Technol.* **29** 025014

IOP Publishing Plasma Sources Science and Technology
Plasma Sources Sci. Technol. **29** (2020) 025014 (13pp) https://doi.org/10.1088/1361-6595/ab6c81

Comparison of electron heating and energy loss mechanisms in an RF plasma jet operated in argon and helium

J Golda[1,2,3], J Held[2] and V Schulz-von der Gathen[2]

[1] Institute of Experimental and Applied Physics, Kiel University, Germany
[2] Experimental Physics II, Ruhr University Bochum, Germany

E-mail: golda@physik.uni-kiel.de

Received 14 November 2019, revised 11 January 2020
Accepted for publication 16 January 2020
Published 14 February 2020

Abstract

The μ-APPJ is a well-investigated atmospheric pressure RF plasma jet. Up to now, it has mainly been operated using helium as feed gas due to stability restrictions. However, the COST-Jet design including precise electrical probes now offers the stability and reproducibility to create equi-operational plasmas in helium as well as in argon. In this publication, we compare fundamental plasma parameters and physical processes inside the COST reference microplasma jet, a capacitively coupled RF atmospheric pressure plasma jet, under operation in argon and in helium. Differences already observable by the naked eye are reflected in differences in the power-voltage characteristic for both gases. Using an electrical model and a power balance, we calculated the electron density and temperature at 0.6 W to be 9×10^{17} m^{-3}, 1.2 eV and 7.8×10^{16} m^{-3}, 1.7 eV for argon and helium, respectively. In case of helium, a considerable part of the discharge power is dissipated in elastic electron-atom collisions, while for argon most of the input power is used for ionization. Phase-resolved optical emission spectroscopy reveals differently pronounced heating mechanisms. Whereas bulk heating is more prominent in argon compared to helium, the opposite trend is observed for sheath heating. This also explains the different behavior observed in the power-voltage characteristics.

Keywords: atmospheric pressure plasma, heating mechanisms, COST-Jet, helium, argon, electron density, electron temperature

1. Introduction

The μ-APPJ is a well established representative of RF-excited atmospheric pressure plasma jets and has been extensively studied throughout the past twenty years. In these studies, helium was usually used as the carrier gas with various molecular admixtures such as oxygen [1], nitrogen [2], water [3], hexamethyldisiloxane (HMDSO) [4] or atomic gases such as argon [5]. However, recent studies have indicated, that an operation in argon might be beneficial for chemical processes like CO_2 conversion [6] and might offer a wider operation range compared to helium [7].

Even if argon is one of the most commonly used operation gases in low temperature plasmas, it proved to be challenging to produce a stable argon discharge in a capacitively coupled discharge geometry. In the past two decades, numerous studies have found that it is easier to generate a homogeneous discharge at atmospheric pressure in helium than in argon [8–10]. Homogeneous argon plasmas are often ignited with the help of helium admixtures [9, 11], as the homogeneous ignition has proven to be difficult. Experimental studies have shown that jet-like sources driven at MHz frequencies are diffuse when operated in helium [12, 13], but tend to form filaments if operated in argon in the exact same discharge geometry [14, 15]. Up to now, there is little literature available on atmospheric pressure argon processes in homogeneous RF discharges. Only when using larger electrode surface areas or higher excitation frequencies, the use of argon as a feed gas in a capacitively coupled geometry basically similar to the μ-APPJ is reported [16, 17].

[3] Author to whom any correspondence should be addressed.

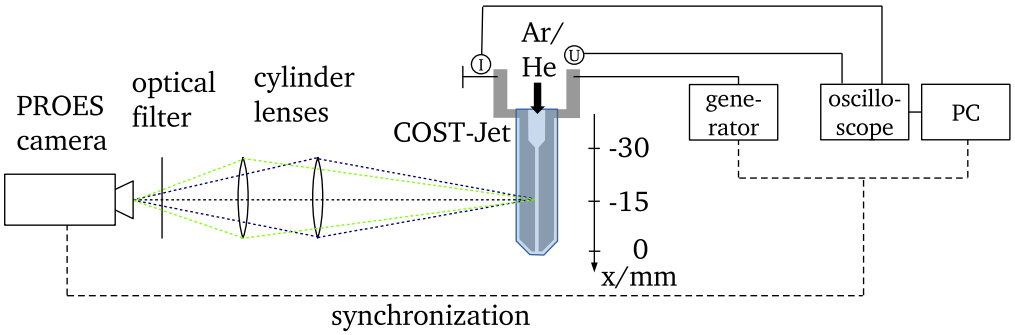

Figure 1. Schematic diagram of the experimental setup for PROES.

Comparing argon and helium plasmas empirically, it has been found that at high $p \cdot d$ values above 10 Torr cm, the breakdown voltage is higher for argon than for helium both for DC and RF electric fields [18, 19]. Moravej *et al* measured RF breakdown curves that show breakdown voltages five times higher for argon than for helium discharges [20]. Additionally, the Townsend first ionization coefficient α/n_g (DC case) for argon is smaller than for helium at reduced electric field strengths below 100 Td [21] as can be calculated from the Townsend ionization coefficients. The typical electric field in the μ-APPJ configuration is of the order of 15 Td [22] and hence, the volumetric ionization rate will be smaller for argon than for helium. This might play a decisive role in the ignition of the discharge.

Besides empirical comparisons of discharges in different operating gases, there are also models of these plasma discharges. Jonkers *et al* compared argon and helium discharges at atmospheric pressure [23]: they found that for a plasma being operated at the same external conditions, an argon plasma has a lower electron temperature and a higher electron density than a helium plasma. A smaller ion mass favors the diffusion of charged particles of the plasma and thus decreases the residence time. Hence, a higher power density is necessary in helium plasmas to obtain the same electron density as in argon plasmas. Additionally, a helium plasma is further from partial local Saha equilibrium than an equi-operational argon plasma.

Thus, both empirical findings and models predict different behavior of homogeneous argon and helium discharges. Yet, a discharge geometry that allows to compare both RF discharges at atmospheric pressure under sufficiently stable and reproducible conditions was not available until now.

This paper extends on previous electrical and optical studies of the μ-APPJ source [24] focusing on the measurement of dissipated power and electron density in atmospheric pressure RF plasma sources. The plasma source as well as the used diagnostic techniques are described in section 2. The macroscopic behavior of the discharges in terms of ignition and dissipated power is analyzed (section 3.1). Fundamental plasma parameters such as electron density (section 3.2.1), electron temperature, loss mechanisms (section 3.2.2) and sheath width (section 3.2.3) are derived. Microscopic differences in electron heating are discussed based on excitation imaging (section 3.3).

2. Experimental

2.1. Atmospheric pressure plasma jet

In this study, we employ the COST Reference Microplasma Jet (COST-Jet), which features the same discharge geometry and excitation scheme as the μ-APPJ [25]. Figure 1 shows a schematic of the COST-Jet device. The plasma in the COST-Jet is generated using a frequency of 13.56 MHz between two 30 mm long, plane-parallel electrodes. One of the electrodes is grounded and the other is connected to the power supply via an LC resonance circuit. Two quartz panes enclose the electrodes, forming a 30 mm × 1 mm × 1 mm discharge channel. Usually, helium is used as the feed gas, at flow rates between 0.25 slpm and 2.00 slpm. Here, we also use pure argon as the feed gas at flow rates between 0.25 slpm and 1.50 slpm. Additionally, we implemented a cold trap to reduce impurities from the feed gas. The COST-Jet features electrical probes for current and voltage that are positioned inside the housing, close to the electrodes. The voltage probe is a pick-up antenna, positioned near the powered electrode. The current probe is a current-sensing resistor with 4.7 Ω. These probes are connected to an oscilloscope (Agilent Technologies DSO7104B). The COST-Jet has been described in more detail elsewhere [25].

2.2. Phase-resolved optical emission spectroscopy

Phase-resolved optical emission spectroscopy (PROES) can give insight into discharge kinetics by synchronizing spectroscopic imaging to the RF excitation cycle of the discharge. The observed emission can be used to qualitatively assess electron excitation processes as well as to calculate quenching coefficients, electron temperature and density [26–28].

In PROES, the electron impact excitation from the ground state $E_{i,0}$ is calculated from the measured spatio-temporal emission. At atmospheric pressures due to collisional de-excitation (quenching), lifetimes of the exited levels are short, and the temporal behavior of the emission is, thus, directly proportional to the excitation rate [29].

Figure 1 illustrates the setup used for phase-resolved optical emission spectroscopy (PROES). The emission produced by the discharge inside the COST-Jet is imaged onto the CCD chip of a gated, intensified charge-coupled device (ICCD) camera (PicoStar HR 16, Lavision). To obtain good spatial resolution for both axes, the aspect ratio of the image

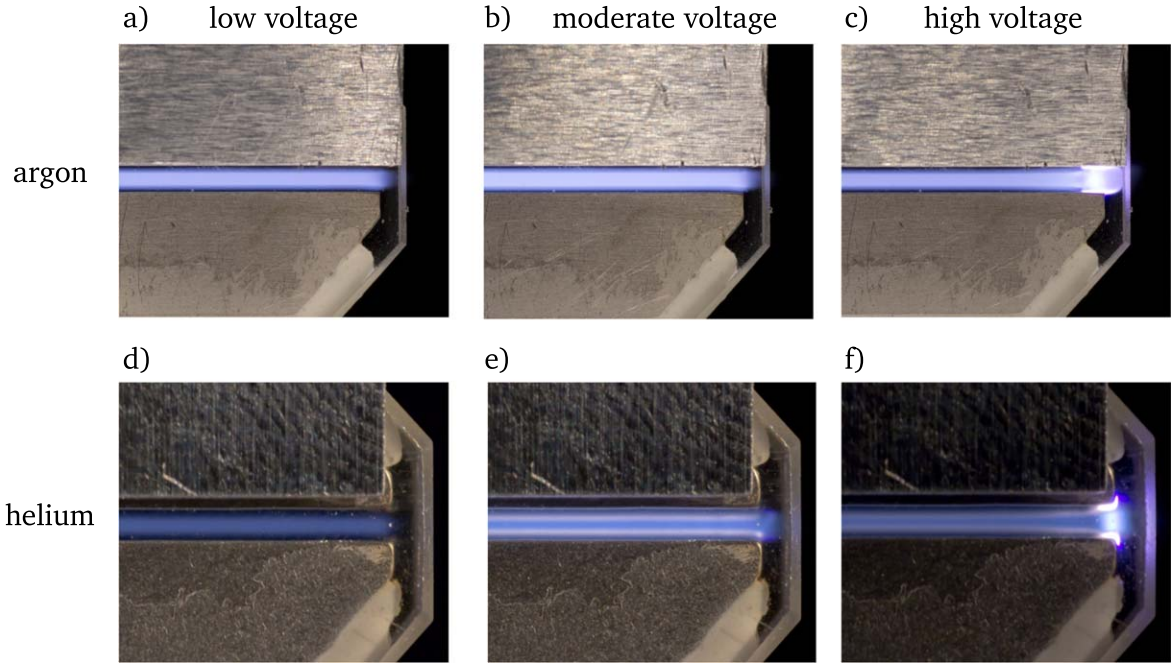

Figure 2. Photographs of the COST-Jet operated in argon (upper row) in (a) homogeneous glow mode at low voltages, (b) homogeneous glow mode at moderate voltages and (c) constricted mode as well as in helium (lower row) in (d) α-like mode at low voltages, (e) γ-like mode at higher voltages and (f) constricted mode. Please note, that the grounded electrode shielding covering the upper electrode only reduces the amount of measured reactive currents to facilitate electrical measurements. Therefore, its position does not have a direct influence on the discharge conditions.

is changed with an anamorphotic lens system. Two cylindrical lenses are used with a focal length of $f = 80$ mm and 110 mm for horizontal and vertical imaging, respectively. In this way, the aspect ratio of the image of the discharge channel is changed from from 1:30 to 4:11 to better fit the dimensions of the CCD chip (512 $\times$ 512 pixel, pixel size 25 μm $\times$ 25 μm). The resulting spatial resolution is 5.5 μm per pixel across the discharge channel and 72 μm per pixel along the discharge channel. Depending on the emission intensity of the respective transition, the camera typically integrates over 1 s to 4 s, while the gate width was set to 1 ns. The synchronization of the gate to the RF voltage is achieved using a customized trigger box and delay generator. The gate delay was increased in steps of 0.72 ns. Thus, one RF cycle is scanned and divided into 103 images which represent the whole cycle. To select a specific emission line, optical filters are inserted into the optical path. Table 1 lists the optical filters and their spectral width (full width at half maximum—FWHM) used during the measurements and the respective observed emission lines. An optical spectrometer (not shown here) was additionally used to ensure that only the listed lines are observed with this PROES setup and other contributions are negligible.

Table 1. Optical filters and corresponding transmission lines used for PROES.

Filter λ_c/nm	FWHM λ_f/nm	Species	Transition	Emission line λ/nm
750	10	Ar I	$2p_1 \rightarrow 1s_2$ and $2p_5 \rightarrow 1s_4$	750.39 and 751.47
706	10	He I	$3^3S \rightarrow 2^3P$	706.5

3. Results and discussions

3.1. Discharge ignition and dissipated power

The difference between the atmospheric pressure RF discharge in argon and helium is already visible by the naked eye: figure 2 shows photographs of the COST-Jet operated in argon (upper row) and helium (lower row) at different voltages. For the helium discharge, ignition is a spontaneous process if a sufficient voltage across the discharge gap is applied. In contrast for the argon discharge, we use a spark vacuum tester to ignite the discharge. Once the discharge is ignited, the complete electrode gap is filled with a homogeneous discharge (abnormal mode) and the emission is dominated by bulk emission (a), (d). For higher voltages, the emission distribution in argon (b) is unchanged, whereas for helium, the emission is more pronounced in the sheath regions (e). If the voltage is further increased for both feed gases, a filament is formed at the tip of the electrodes (c), (f).

The difference between the argon and helium discharge visible in the photographs is also reflected in the dissipated power: figure 3 shows power-voltage characteristics of the discharge operated at gas flow rates of 400 sccm argon (a) and 1000 sccm helium (b). To provide a controlled atmosphere and reduce fluctuations, the experiments were performed in a gas chamber that was pumped down prior to the experiments, refilled with the feed gas and operated at a pressure of

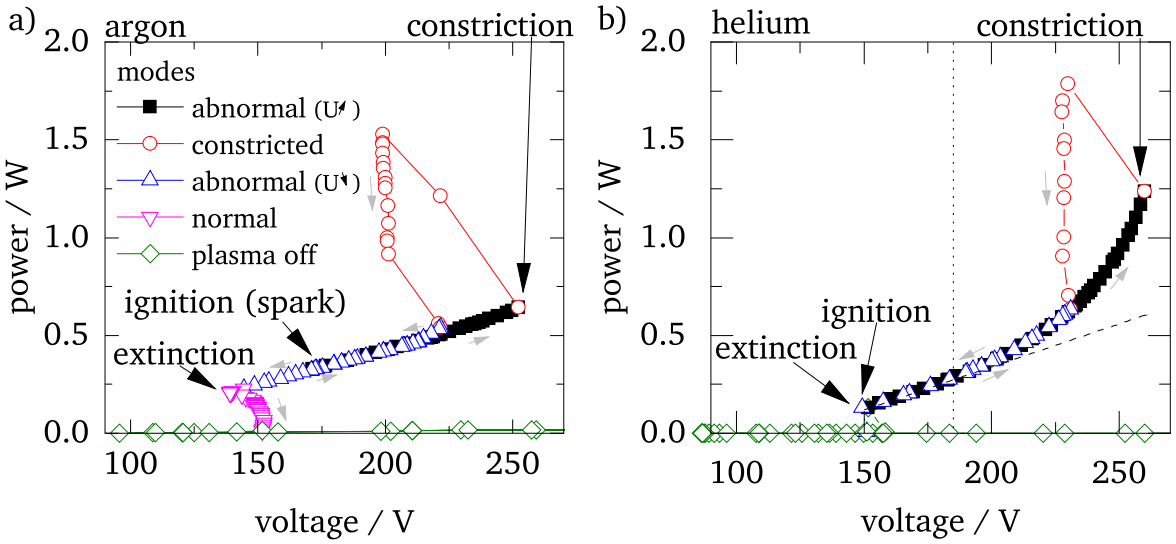

Figure 3. Power dissipated in the (a) argon and in the (b) helium plasma discharge depending on discharge voltage (pressure 990 mbar, gas flow rate 400 sccm and 1000 sccm, respectively). The black dashed line is the linear part of the power curve as described in the text.

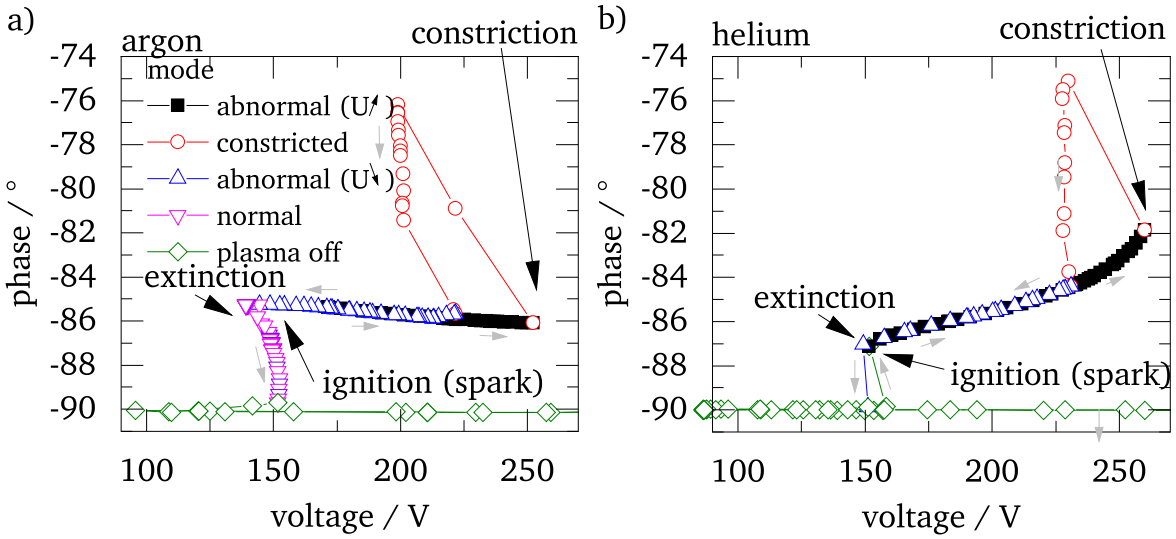

Figure 4. Phase angle of the (a) argon and the (b) helium discharge depending on voltage (pressure 990 mbar, gas flow rate 400 sccm and 1000 sccm, respectively).

990 mbar. The results are comparable to experiments at ambient atmosphere. The behavior depicted is similar for both discharges: when the voltage is increased, the dissipated electrical power increases. When a threshold voltage is reached the filament is formed (figure 2(c), (f)) leading to an instantaneous power increase and a decrease in voltage. If the voltage is then lowered the discharge switches back into the homogeneous mode. If the voltage is further decreased the dissipated power decreases and the discharge is subsequently extinguished. The difference between the discharges can be observed in the slope between voltage and power: whereas the relationship is fairly linear for argon as the feed gas, there seems to be an additional power dissipation term for helium at higher voltages.

To investigate this difference, figure 4 shows the phase angle difference between voltage and current, for both feed gases. For both discharges, the plasma-off phase angle is $-90\,^{\circ}$ corresponding to an ideal capacitor. If the discharge is ignited, both discharges show a resistive component in the phase angle. But strikingly, the phase angle is decreasing for increasing voltage for the argon discharge and increasing for the helium discharge. The cause and effect of this difference is analyzed based on an electrical model and will be discussed in the following section.

3.2. Plasma parameters from an electrical model

The dissipated power in the plasma is the motor of all discharge processes. Therefore, a detailed analysis of the power using a global model can give insight into fundamental plasma parameters such as the electron density or temperature. To investigate the differences between the argon and the helium plasma, we used a simple global model that consist of a capacitor representing the sheath in series with a resistor

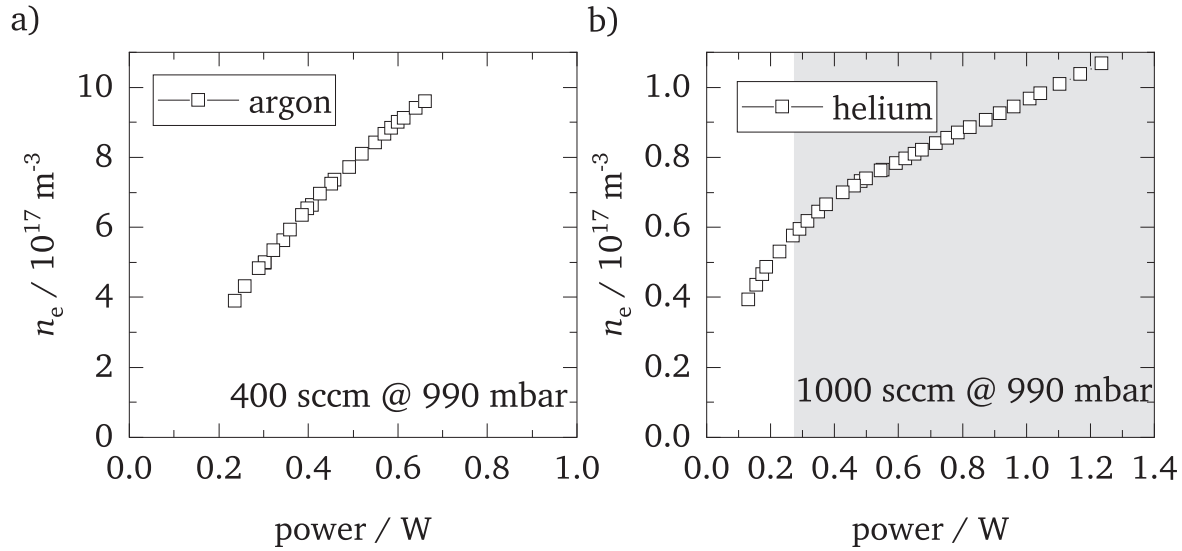

Figure 5. Electron density as function of dissipated power for (a) argon discharge and for (b) helium discharge (pressure 990 mbar, gas flow rate 400 sccm and 1000 sccm, respectively). Note the different scales. Shaded area denotes limited applicability of the electrical model as described in [24].

and a capacitor representing the plasma bulk. Specific aspects of the calculation and detailed comparisons to further diagnostics and simulations have already been published in a separate publication [24] and confirm the trends and absolute values. Based on the dissipated power, it is possible to establish equi-operational plasmas and thus directly compare the two feed gases [23].

3.2.1. Electron density. The electron density deduced from the model can be directly calculated from the bulk resistance representing the plasma bulk derived from the data in figure 4 via [24, 30]

$$n_e = \frac{l - 2s_0}{AR_b}\frac{\nu_m m_e}{e^2}, \tag{1}$$

where l is the inter-electrode distance (1 mm for the COST-Jet) and R_b the plasma bulk resistance, s_0 the sheath thickness, A the electrode surface, m_e the electron mass and e the elementary charge. For argon and helium at atmospheric pressure, the electron-neutral collision frequency is $\nu_m = 4.03 \times 10^{12}$ s^{-1} and 1.52×10^{12} s^{-1}, respectively [31].

Figure 5 shows the calculated electron density as a function of dissipated power for a 400 sccm argon discharge 5(a) and a 1000 sccm helium discharge 5(b). The lower gas flow rate of argon was chosen to increase discharge stability but does not have an influence on electrical characteristics. In both cases, the calculated electron density exhibits a monotonous increase with dissipated power. However, at a given discharge power, the electron density in the argon discharge is approximately one order of magnitude higher than in the helium discharge. This implies that in helium a large part of the available energy is not used for ionization but instead invested in another process. The influence of Penning ionization was estimated to be negligible as the amount of impurities in the discharge was reduced by conducting experiments in a gas chamber with controlled atmosphere. A likely candidate is electron heating, as the higher excitation energy, e.g. to excite metastables, as well as higher ionization energy of helium requires a higher electron temperature to sustain the discharge.

3.2.2. Electron temperature. Using a simplified zero-dimensional power balance model for free electrons, a rough estimate of the average electron temperature in the bulk plasma can be performed by relating the measured power density ϵ to the power per unit of volume that is lost by inelastic and elastic electron collisions [23]:

$$\epsilon = n_e \frac{p}{k_B T_g} S_{CRM} I_1 + n_e \times \left[n_+ \langle \sigma^m_{ei} \nu_e \rangle + \frac{p}{k_B T_g} \langle \sigma^m_{ea} \nu_e \rangle \right] \cdot \frac{2m_e}{M} \frac{3}{2} k_B (T_e - T_g), \tag{2}$$

with:

ϵ	= Power density
m_e	= Electron mass
M	= Atomic mass
ϵ	= Power density
n_e	= Electron density
n_+	= Ion density
$p/(k_B\ T_g)$	= Atom density (Dalton's law)
I_1	= Ionization energy
T_e	= Electron temperature
T_g	= Gas temperature
S_{CRM}	= Ionization rate coefficient

The ionization rate coefficient is deduced from collisional radiative models (CRM). $\langle \sigma^m_{ei} \nu_e \rangle$ and $\langle \sigma^m_{ea} \nu_e \rangle$ are the electron-ion and electron-atom collision rate coefficients for momentum transfer averaged over the electron energy distribution function.

The first term in equation (2) describes energy loss due to ionization; the second and third term due to elastic electron-

ion and electron-atom collisions, respectively. The energy required to heat cold electrons generated in the ionization process and energy losses due to radiation were omitted. To calculate the electron temperature, realistic numerical values must be estimated for all variables in equation (2). All variables were estimated for a dissipated power of 0.6 W which corresponds to a power density of 2×10^7 W m^{-3}:

- For an estimate of the argon *neutral gas temperature* T_g, the temperature in the effluent was measured using laser schlieren deflectrometry (LSD) [32, 33] and cross-checked using a thermocouple in the effluent as a function of the distance to the gas exit. Both methods show very good agreement in the trends, with a difference in the absolute values of about 20 K. This difference is most likely due to the laser schlieren deflectrometry measuring the peak temperature, whereas the thermocouple measures integrated values due to the spatial dimensions of the probe tip. Therefore, the averaged value between the two measurements was used. The measurements performed in the effluent were extrapolated into the bulk plasma and a value of $T_g = 350$ K was obtained.

  For the helium discharge, the neutral gas temperature has previously been measured using thermocouples embedded into the discharge channel and compared to simulations [34]. From these measurements, we estimated a value of $T_g = 350$ K for helium, as well.
- For an estimate of the *ionization rate coefficients* in the power balance, analytical expressions from fits by Jonkers *et al* [23] to results from collisional radiative models were used with $\hat{T}_e$ and n_e in eV and m^{-3}:

$$S_{\mathrm{CRM}}^{\mathrm{Ar}} = 7.34 \cdot 10^{-15} \sqrt{\hat{T}_e} \exp\left(\frac{-12.06}{\hat{T}_e}\right) [\mathrm{m^3\ s^{-1}}]$$

$$S_{\mathrm{CRM}}^{\mathrm{He}} = 3.15 \cdot 10^{-15} \sqrt{\hat{T}_e} \exp\left(\frac{-19.38}{\hat{T}_e}\right) [\mathrm{m^3\ s^{-1}}]. \quad (3)$$

$$\langle \sigma_{\mathrm{ei}}^{\mathrm{m}} \nu_e \rangle = \frac{2.91 \cdot 10^{-12}}{\hat{T}_e^{\frac{3}{2}}} \times \ln\left(1.55 \cdot 10^{13} \sqrt{\frac{\hat{T}_e^3}{n_e}}\right) [\mathrm{m^3\ s^{-1}}], \quad (4)$$

- The electron-ion and electron-atom *collision rate coefficients* for momentum transfer were obtained by Jonkers *et al*, by fitting cross sections and integrating over a Maxwellian EEDF [23] with $\hat{T}_e$ and n_e in eV and m^{-3}.

$$\langle \sigma_{\mathrm{ea}}^{\mathrm{m}} \nu_e \rangle^{\mathrm{Ar}} = (0.084 + 0.537\, \hat{T}_e + 1.192\, \hat{T}_e^2) \cdot 10^{-14} \quad [\mathrm{m^3\ s^{-1}}] \quad (5)$$

$$\langle \sigma_{\mathrm{ea}}^{\mathrm{m}} \nu_e \rangle^{\mathrm{He}} = (2.21 + 2.59\, \hat{T}_e - 0.344\, \hat{T}_e^2) \cdot 10^{-14} \quad [\mathrm{m^3\ s^{-1}}] \quad (6)$$

Using these values and the electron densities at 0.6 W calculated in section 3.2.1, we can estimate the electron temperature in the argon and helium plasma by solving equation (2) to be 1.20 eV and 1.70 eV, respectively. As anticipated, the electron temperature in helium is approximately 40% higher than in argon. However, the absolute values are surprisingly low. For argon, this might be due to an overestimation of the ionization coefficient. Strictly speaking, equations (3) and (4) are only valid for electron densities above 1×10^{19} m^{-3}. Below that value, the ionization coefficients also decrease with decreasing electron density [35]. Additionally, the collisional radiative models used for the fit of equation (3) and (4) are not optimized for high neutral densities and an extremely low degree of ionization, i.e. they do not account for excited molecular dimer levels and molecular ions [36]. The gas temperatures only have a minor effect on the results. These calculated electron temperatures are only a general orientation, since also all of the collision frequencies were calculated assuming Maxwellian electron energy distribution functions which are usually not present in cold atmospheric pressure plasmas [37, 38]. However, the calculated electron temperatures do show reasonable trends and reflect the physical differences of the two operating gases.

To highlight the differences between the two operating gases, the contributions to the power balance will be separated. Figure 6 shows the three addends of equation (2) as a function of the electron temperature for the argon and the helium discharge. As illustrated in figure 6(a), the dominating term in the argon power balance for power densities above 2×10^7 W m^{-3} (marked by a horizontal dashed line) is energy loss due to ionization whereas elastic collisions, in particular for electron-ion collisions, are comparably small. Ionization compensates the losses of free electrons due to diffusion and recombination by production of charged species. Neglecting the two smaller energy loss terms, equation (2) simplifies to:

$$n_e \approx \frac{\epsilon}{I_1} \frac{k_B T_g}{p S_{\mathrm{CRM}}}. \quad (7)$$

Consequently, the electron density is proportional to the power density for the argon discharge as observed in figure 5.

In contrast, figure 6(b) shows that for helium, the term representing elastic electron-atom collisions dominates. Only at power densities above 3×10^8 W m^{-3}, the ionization term takes over (not shown here). This difference is due to the different cross sections and atomic masses of helium and argon. As argon has a lower ionization threshold, the ionization term in equation (2) is lower in helium. Additionally, the elastic electron-atom collision rate is smaller for argon than for helium due to the Ramsauer minimum at low electron energies (compare cross section data by Phelps [39]) and the electron density in argon is one order of magnitude higher compared to helium, as demonstrated in the previous section. Thus, the elastic electron-atom collision losses are higher in helium than in argon for electron energies below 3 eV.

Consequently, the electron density for helium can be simplified to being proportional to the power density as done

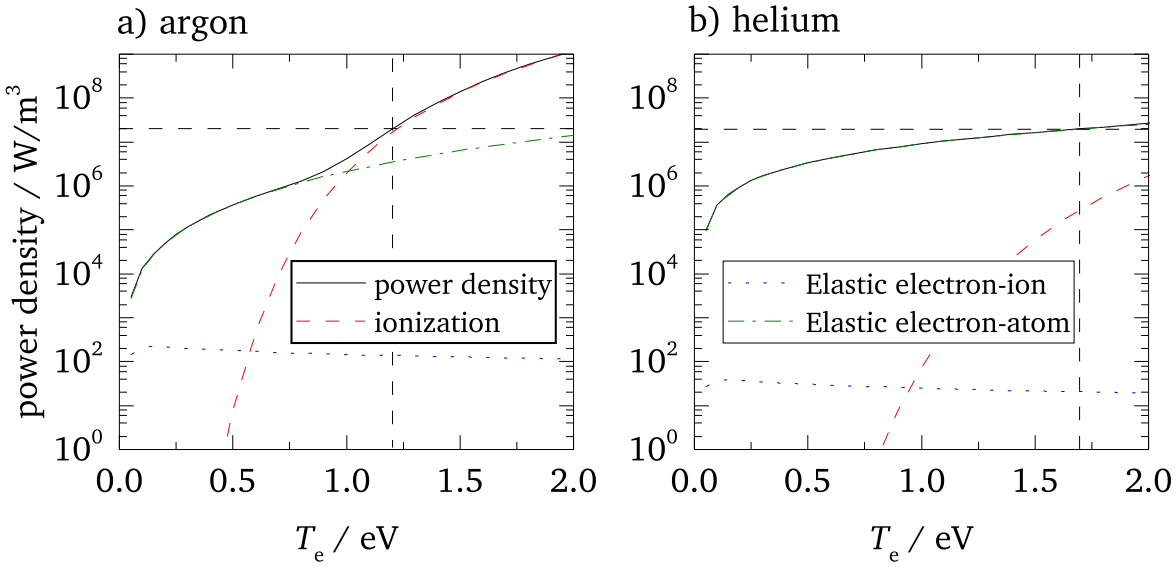

Figure 6. Components of the power balance equation (2). Horizontal dashed lines indicate the power density in the COST-Jet at a dissipated power of 0.6 W, vertical dashed lines indicate the corresponding electron temperature.

by many other authors [40, 41]:

$$n_e \approx \frac{M}{3m_e}\frac{k_B T_g}{p}\frac{\epsilon}{\langle\sigma^m_{ea}\nu_e\rangle k_B(T_e - T_g)}. \quad (8)$$

However, the electron density calculated from the impedance measurement as illustrated in figure 5(b) does not show linear behavior. Instead, it begins to increase linearly at low powers and then exhibits a less steep power dependence above about 0.3 W. Especially considering the increasing gas temperature with increasing power, as demonstrated for helium in literature [34], the electron density should increase over-proportional. This demonstrates, that the circuit model for helium is only valid at low dissipated powers.

Nevertheless, the general difference in electron energy loss for both discharges can be explained using this simple energy balance: in argon, nearly all of the energy put into the discharge is used for ionization. This leads to a comparatively high electron density ($9 \times 10^{17}\,\mathrm{m}^{-3}$), but low electron temperature of (1.2 eV) at a power of 0.6 W. For an equi-operational helium discharge, most electron energy is lost in electron-atom collisions. To still sustain the discharge, the electron temperature is higher (1.7 eV) at a low electron density of $0.8 \times 10^{17}\,\mathrm{m}^{-3}$. Surprisingly, this is not reflected in the measured gas temperatures: Within measurement uncertainties, the two equi-operational discharges both exhibit a gas temperature of 350 K. As we could only measure the gas temperature in the effluent, the energy stored in charge carriers and excited states is transformed into kinetic energy in the effluent, e.g. by collisional quenching and recombination, thus heating the gas. However, the parameter gas temperature only has a minor influence on the electron temperature derived from equation (2) and variation of the temperature does not change the results notably.

However, the trends observed for the two characteristic plasma bulk parameters electron density and electron temperature are identical for argon and helium, so they do not explain the differences in the phase characteristic shown above (see figure 4). Therefore, we will investigate the sheath properties of both plasma discharges.

3.2.3. Sheath width. According to the hybrid model by Lazzaroni *et al* [42], the sheath width depends on the electron temperature as well as on the ratio of the electron losses by inelastic and elastic processes. Whereas the electron temperature is lower for argon than for helium, the ratio of inelastic to elastic losses is higher. Therefore, trends of the absolute sheath thickness and the differences between the gases cannot easily be predicted.

Therefore, we have again consulted the global electrical model. The sheath width can be deduced from the capacitor representing the sheath and gives reasonable results when compared to simple photographs [24]. In figure 7, the sheath width is shown for the argon as well as for the helium discharge. Again, both discharge exhibit the same trend in dependence of the dissipated power. With increasing dissipated power the sheath width decreases monotonously. For both plasma discharges, the sheath width varies between 350 and 210 µm. The sheath width in the argon plasma is slightly smaller than in the helium plasma. Both values show excellent agreement with results from modeling by Lazzaroni and Chabert [7] for argon and Waskoenig [43] for helium. Nevertheless, the trends observed for the sheath thickness are identical for argon and helium. Therefore, we will investigate the properties of both plasma discharges switching from global, time-integrated to local, phase-resolved diagnostics to analyze the electron dynamics in both plasma discharges as presented in the following section.

3.3. Electron heating mechanisms

The global measurements presented in section 3.1 using electrical measurements revealed differences in the characteristics of dissipated power in the argon and helium

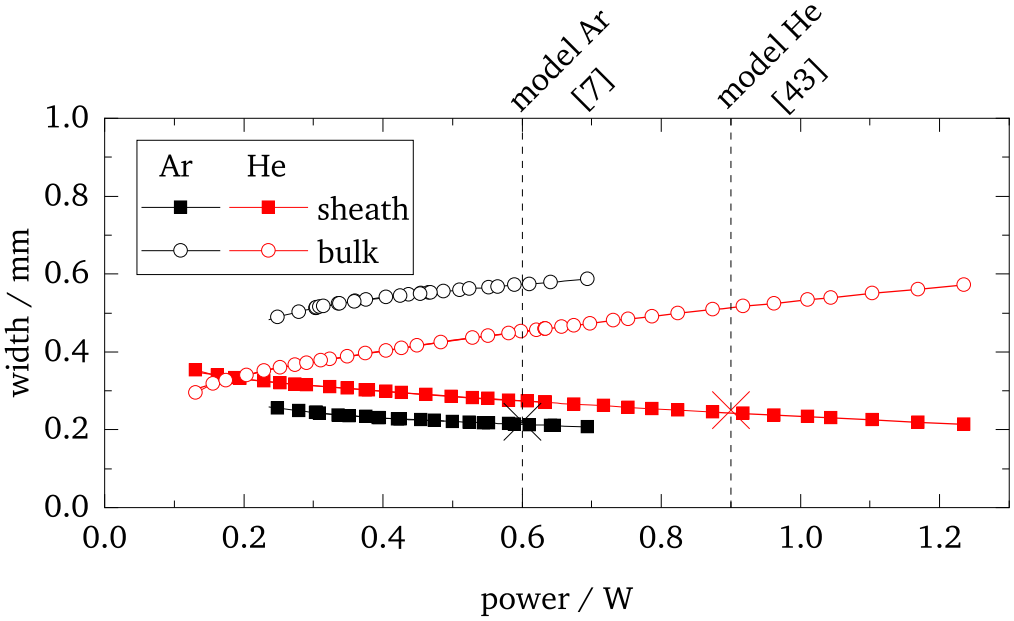

Figure 7. Bulk and sheath width in the abnormal mode as a function of the dissipated power for argon (black symbols) and helium (red symbols) discharge. The dashed lines mark modeling results from literature [7, 43].

discharge leading to an opposing behavior of the phase difference between current and voltage. This behavior suggests that the temporal and spatial profile of the electron heating and ionization rates is affected. To identify different electron heating mechanisms, the time-resolved emission in the argon and helium plasma is compared at different dissipated power values.

Figure 8 shows discharge emission structures in one-dimensional phase-resolved plots within one RF-period between the electrodes for the argon and the helium discharge. The abscissa comprises a full RF period (74 ns). To guide the eye, the estimated position of the plasma sheath edge is indicated by black lines. These plots originate from the central lateral position ($x = -15$ mm) of the discharge channel as defined in figure 1.

For argon, the emission at 750 nm and for helium at 706 nm is shown at a typical low (upper row), moderate (lower row) and high power of 260 mW, 540 mW and 1000 mW, respectively. These isolated emission lines are expected to reflect the ionization dynamics in the discharge. As expected, the absolute intensity rises with increasing applied voltage (not shown here). However, to emphasize the structure, these images are normalized to their respective maximum.

3.3.1. Emission structures in the argon discharge. Figure 8(a) shows that the emission is strongly time modulated. The measurements reveal two intensity maxima within one RF half-period (labeled with I and II, respectively). This is an indicator for a high electron energy at the position close the sheath edge, since the electron impact excitation of the $2p_1$ state requires an electron energy of 13.5 eV. Comparing (a) to (c), the images reveal that the principal excitation scheme is the same for elevated powers except for the change in time indicated by vertical dashed lines. For higher operation voltages, emission maximum I appears approximately 6.5 ns earlier in phase than for low voltages. This time shift is less pronounced for emission maximum II. Additionally, a faint, third emission maximum (marked with III) begins to develop which is approximately as bright as the second maximum (II) but much less bright than maximum I.

3.3.2. Emission structures in the helium discharge. In helium (see figure 8(b)), the same emission structures can be observed but are differently pronounced: Initially, only two emission structures (I and II) are visible. With increasing dissipated power, the intensity of maximum III increases strongly. At 540 mW, maximum III is already more prominent than emission maximum I. For helium, the dissipated power could be even increased to 1000 mW (see figure 8(e)), where the argon discharge would already form a filament. At this power, emission structure III is clearly dominating the emission pattern, while emission maxima I and II are only faintly visible. This is an indication for a complete mode change in the helium case, whereas for argon only a small change was observed.

The emission structures in helium are well documented in the literature (compare [44–46]). As the emission structures observed at atmospheric pressure closely resembles those observed in low temperature plasmas, the nomenclature is often adopted as α-mode (maxima I/II) and γ-mode (maximum III). However at atmospheric pressure, the underlying processes are completely different and will therefore briefly be described in the following.

In low pressure plasmas, the first maximum is attributed to energetic electrons during sheath expansion. The second maximum is induced by a momentary reversal of the local electric field during sheath collapse [47]. However at atmospheric pressure, no field reversal was observed in

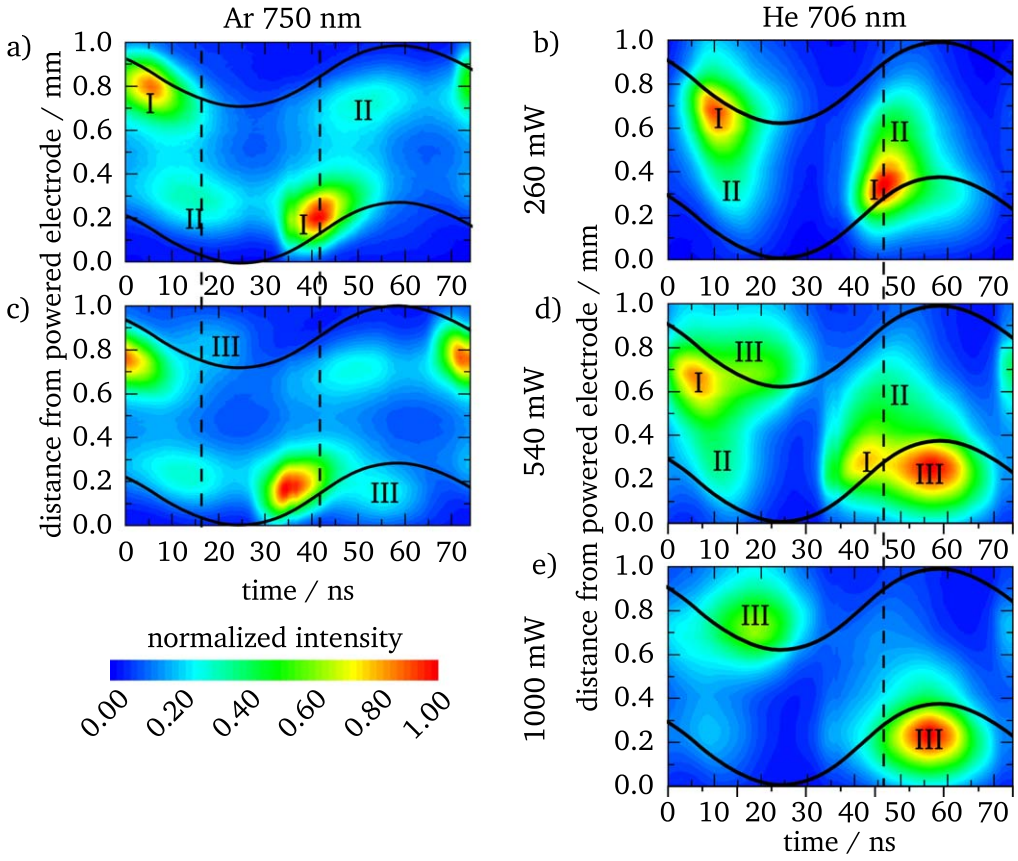

Figure 8. Normalized phase-resolved emission plots of the argon 750 nm emission line (left) and the helium 706 nm emission line (right) operated at 260 mW (a), (b), 540 mW (c), (d), and 1000 mW (e).

numerical simulations [44, 45] but instead an enhanced electric field without changes in polarity.

According to Hemke *et al* [44], ionization during sheath expansion is caused by a high bulk electric field that has local extrema at the sheath edges. This electric field is predominantly a drift field due to the low conductivity of the bulk discharge. According to Liu *et al* [45], in contrast to low pressure helium plasmas, the emission structures indicate that the electrons are not only heated during the sheath expansion [21], but may also be considerably heated during the sheath retreat. The additional heating is caused by a field-enhanced region in front of the retreating sheath. A small number of electrons are not able to follow the retreating sheath due to collisions at high pressure. Those electrons accumulate and create a region of negative space charge. Thus, a self-consistent electric field forms that accelerates the electrons towards the electrode, heating them in the process. As the current signal precedes the voltage signal by approximately 90° (compare figure 4), the emission maxima (I + II) are also related to the maxima of the current magnitude [16]. Hemke *et al* [44] named this effect of Ohmic bulk heating of electrons the Ω-mode. However, this designation has not been consistently accepted, as most other authors still continue to refer to this mode as α-mode.

The emission structures of excited argon atoms closely resemble measurements and simulations by Dünnbier *et al*, who conducted PROES at a similar discharge geometry, but at a higher excitation frequency of 27 MHz [16]. Since they used a wider electrode gap and a higher frequency, they observed more concise emission structures and a rather faint emission maximum II due to the smaller oscillation amplitude of the charged species. We also measured the emission at the 811 nm line (not shown here) which also shows the same trends as measured by Dünnbier *et al*.

3.3.3. Differences between argon and helium discharge. Comparing the emission pattern in argon and helium, the observations fit very well to the expectations derived from the observations of measurements in helium as illustrated in figure 8 (compare also [32, 33, 46]). The emission structures are mainly similar but exhibit slight differences. In helium, emission maxima I and II are not clearly separated and emission maximum II is much less pronounced than in argon. This is probably due to the higher collision cross section for momentum transfer in argon for high electron energies. Additionally, due to their lower mass, the mobility of helium ions is higher than that of argon ions. Therefore, the electrons can easily follow the electrical field and are not slowed down by ambipolar diffusion.

The third maximum can be attributed in time to the maximum of the discharge voltage, where the electric field and the sheath amplitude is largest in the cathode region. Therefore, it is attributed to secondary electron processes. Consequently, following the low pressure plasma

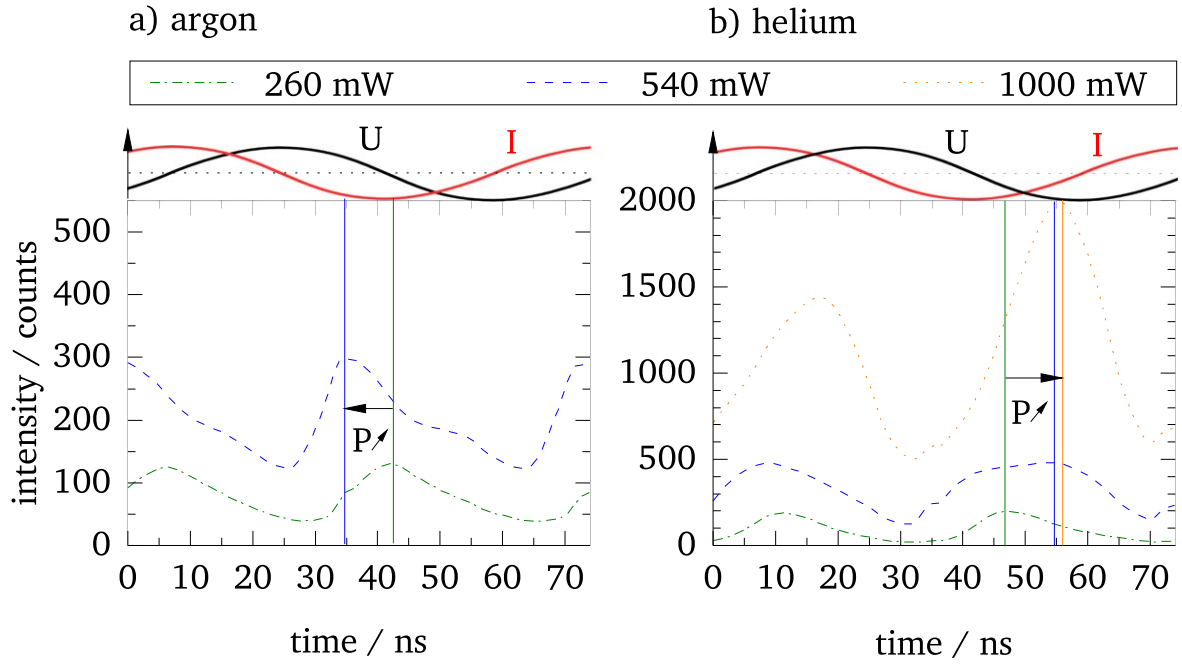

Figure 9. Development of the intensity integrated across the discharge gap: (a) 750 nm intensity of the argon discharge and the (b) 706 nm intensity of the helium discharge at different power values corresponding to figure 8.

nomenclature, it is referred to as γ-mode. However, at atmospheric pressure and in particular using molecular feed gas admixtures, also charge transfer, electron reflection and Penning ionization processes can play a decisive role. Therefore, Bischoff *et al* also call it Penning-mode [29].

In helium, these secondary electron processes are more prominent than in argon. For low velocities of impinging particles, the secondary electron emission yield is nearly independent of this velocity. This is because, the electron emission occurs primarily due to transfer of the incoming ion or atom's potential energy to an electron in the target [48–50]. Considering that the ionization energies of Ar^+ and He^+ are 15.76 eV and 24.59 eV, respectively [51], i.e. they differ by 56%, one might expect the potential secondary electron yield to be considerably different. Accordingly, Hagstrum measured the secondary electron emission yield for helium and argon bombarding a clean tungsten surface [49]. At an ion energy of around 10 eV, the secondary electron emission yield of helium is more than twice that of argon. Therefore, secondary electron emission by impinging particles likely plays a larger role in the helium discharge than in argon. However, emission maximum III is not only due to electron avalanches initiated by secondary electrons produced at the electrode surface. Instead, other processes also contribute: (i) photoionization in the sheaths, (ii) pooling reactions near the electrode surface between metastables and excimers ($Ar^* + Ar^* \Rightarrow Ar^+ + e^- + Ar$, $Ar_2^* + Ar_2^* \Rightarrow Ar_2^+ + 2Ar + e^-$). Metastables and excimers have already been identified, e.g. in VUV spectra [52, 53]. These processes are a source of non-thermal electrons. If these electrons are created inside the sheath, they are strongly accelerated by the high electric field. Since the potential energies of excited helium levels and thus the kinetic energy of the released electrons and photons is higher than in argon, re-excitation reactions and thus heating of the discharge is supported.

These differences in heating mechanisms agree with observations from the global electrical measurements described in section 3.1, as they explain the inverse phase dependence on the discharge voltage shown in figures 4(a) and (b): whereas the absolute value of the phase difference between current and voltage is increasing with higher discharge voltage for argon, it is decreasing for helium. This can be explained by the change in the phase-resolved emission pattern: figure 9 shows the temporal development of the intensity integrated across the discharge gap of the (a) 750 nm line of the argon discharge and the (b) 706 nm line of the helium discharge at different power values. According to simulations by Hemke *et al* [44] and Dünnbier *et al* [16], the emission maxima correspond to the maximum discharge current amplitude. Therefore, the emission intensity is a measure for the absolute value of the discharge current as qualitatively plotted above the graph. Additionally, the qualitative discharge voltage behavior can be deduced from the sheath oscillations and is also indicated above the graphs.

The maxima of the emission for each power level are marked in the graphs by vertical lines. With increasing power, the emission maximum (and thus the current) of the argon discharge is shifted to earlier times in the cycle. This corresponds to an increase of the absolute value of the phase difference as observed in figure 4(a). In contrast, the emission maximum (and thus the current) of the helium discharge is shifted to later times in the cycle. This results in a decrease of the absolute value of the phase difference with increasing power as observed in figure 4(b). So the microscopic differences in heating mechanisms result in a macroscopic

difference of the phase behavior observed with the global measurements.

This behavior also supports the measurements presented in section 3.1: for argon, the dissipated power rises linearly with increasing voltage. However for helium, an additional power term is observed that might be explained by these secondary electron processes causing additional sheath heating.

4. Conclusion

In this publication, we compare fundamental plasma parameters and physical processes such as electron heating and energy loss mechanisms of a capacitively coupled RF atmospheric pressure discharge operated in argon and in helium. A first comparison via photographs reveals differences in the emission structures with increasing applied voltage between argon and helium that is also reflected in the power and phase characteristics. Opposite to the argon discharge, the helium discharge exhibits pronounced emission zones at the sheath edges as well as an additional loss term in the power characteristics and a decrease in phase angle in abnormal mode with increasing voltage and power.

To explain this behavior, we deduced the electron density from a simple electrical model to monotoneously increase with dissipated power for both feed gases. At a given discharge power, the electron density in the argon discharge is approximately one order of magnitude higher than in the helium discharge.

To analyze the electron temperature, we used a simple energy balance. In argon, nearly all of the energy put into the discharge is used for ionization. This leads to a comparatively high electron density of $9 \times 10^{17}\,\mathrm{m}^{-3}$, but low electron temperature of 1.2 eV at a power of 0.6 W. For an equi-operational helium discharge, most of the electron energy is lost in elastic electron-atom collisions. To still sustain the discharge, the electron temperature is higher (1.7 eV) at a low electron density of $7.8 \times 10^{16}\,\mathrm{m}^{-3}$.

The phase-resolved emission structures observed in the argon discharge using PROES roughly resemble the structures observed in the helium discharge but are differently pronounced. Whereas the emission maximum in front of the retreating sheath is more prominent in argon compared to helium, the opposite trend is observed for the emission maximum in the sheath. As the emission maximum in front of the retreating sheath is due to the electrons not being able to follow the retreating sheath, this is probably caused by the higher mobility of helium ions. The emission maximum in the sheath is caused by secondary electron processes in the sheath. Therefore, it is stronger in helium, as the potential energy levels of excited states are higher compared to argon. Assuming these emission maxima being a measure for the absolute value of the current amplitude, this explains the opposing behavior observed in the phase-power characteristics. This observation represents the bridge between the microscopic differences in heating mechanisms and the macroscopic difference in the global, electrical measurements.

Based on these findings regarding electron density and temperature, we propose that the use of argon instead of helium as feed gas for the dissociation of molecular admixtures such as CO_2 might be advantageous for the conversion rate. The electron temperature in argon is lower than in helium but the electron energy is still sufficient to initiate dissociation of molecules, e.g. CO_2. However, the electron density is significantly higher than in helium, thus increasing the reaction rate and consequently the conversion rate. This might contribute to the interpretation of recently published results by Stewig *et al* [6] on CO_2 conversion rates. Especially promising is the combination with other adaptations, such as modifying the excitation voltage waveform and frequency to modify the temporal and spatial appearance of the heating modes in order to tailor the discharge for improved chemical applications [16, 54].

Acknowledgments

The authors would like to thank Jan Schäfer and Rüdiger Foest from INP Greifswald for help with Laser Schlieren Deflectrometry measurements. This work was funded by the DFG within PAK 816 PlaCiD *Plasma-cell interactions in Dermatology* and CRC 1316 *Transient Atmospheric Plasmas: from plasmas to liquids to solids*.

ORCID iDs

J Golda https://orcid.org/0000-0003-2344-2146
J Held https://orcid.org/0000-0003-1206-7504
V Schulz-von der Gathen https://orcid.org/0000-0002-7182-3253

References

[1] Knake N, Niemi K, Reuter S, Schulz-von der Gathen V and Winter J 2008 Absolute atomic oxygen density profiles in the discharge core of a microscale atmospheric pressure plasma jet *Appl. Phys. Lett.* **93** 131503
[2] Niemi K, O'Connell D, de Oliveira N, Joyeux D, Nahon L, Booth J P and Gans T 2013 Absolute atomic oxygen and nitrogen densities in radio-frequency driven atmospheric pressure cold plasmas: synchrotron vacuum ultra-violet high-resolution Fourier-transform absorption measurements *Appl. Phys. Lett.* **103** 034102
[3] Benedikt J, Schröder D, Schneider S, Willems G, Pajdarová A, Vlček J and Schulz-von der Gathen V 2016 Absolute OH and O radical densities in effluent of a He/H_2O micro-scaled atmospheric pressure plasma jet *Plasma Sources Sci. Technol.* **25** 045013
[4] Rügner K, Reuter R, Ellerweg D, de los Arcos T, von Keudell A and Benedikt J 2013 Insight into the reaction scheme of SiO_2 film deposition at atmospheric pressure *Plasma Process. Polym.* **10** 1061–73
[5] Niermann B, Böke M, Sadeghi N and Winter J 2010 Space resolved density measurements of argon and helium metastable atoms in radio-frequency generated He–Ar micro-plasmas *Eur. Phys. J.* D **60** 489–95

[6] Stewig C, Schüttler S, Urbanietz T, Boeke M and von Keudell A 2019 Excitation and dissociation of CO_2 heavily diluted in noble gas atmospheric pressure plasma *J. Phys. D: Appl. Phys.* **53** 125205

[7] Lazzaroni C and Chabert P 2016 A comparison between micro hollow cathode discharges and atmospheric pressure plasma jets in Ar/O_2 gas mixtures *Plasma Sources Sci. Technol.* **25** 065015

[8] Benedikt J, Hofmann S, Knake N, Böttner H, Reuter R, von Keudell A and Schulz-von der Gathen V 2010 Phase resolved optical emission spectroscopy of coaxial microplasma jet operated with He and Ar *Eur. Phys. J.* D **60** 539–46

[9] Benedikt J, Raballand V, Yanguas-Gil A, Focke K and von Keudell A 2007 Thin film deposition by means of atmospheric pressure microplasma jet *Plasma Phys. Control. Fusion* **49** B419

[10] Iza F, Kim G J, Lee S M, Lee J K, Walsh J L, Zhang Y T and Kong M G 2008 Microplasmas: sources, particle kinetics, and biomedical applications *Plasma Process. Polym.* **5** 322–44

[11] Moon S Y, Han J and Choe W 2006 Control of radio-frequency atmospheric pressure argon plasma characteristics by helium gas mixing *Phys. Plasmas* **13** 013504

[12] Schmidt-Bleker A, Norberg S A, Winter J, Johnsen E, Reuter S, Weltmann K D and Kushner M J 2015 Propagation mechanisms of guided streamers in plasma jets: the influence of electronegativity of the surrounding gas *Plasma Sources Sci. Technol.* **24** 035022

[13] Winter J, Santos Sousa J, Sadeghi N, Schmidt-Bleker A, Reuter S and Puech V 2015 The spatio-temporal distribution of He (2^3S_1) metastable atoms in a MHz-driven helium plasma jet is influenced by the oxygen/nitrogen ratio of the surrounding atmosphere *Plasma Sources Sci. Technol.* **24** 025015

[14] Iseni S, Schmidt-Bleker A, Winter J, Weltmann K-D and Reuter S 2014 Atmospheric pressure streamer follows the turbulent argon air boundary in a MHz argon plasma jet investigated by OH-tracer PLIF spectroscopy *J. Phys. D: Appl. Phys.* **47** 152001

[15] Reuter S, Schmidt-Bleker A, Iseni S, Winter J and Weltmann K-D 2014 On the bullet-streamer dualism *IEEE Trans. Plasma Sci.* **42** 2428–9

[16] Dünnbier M, Becker M M, Iseni S, Bansemer R, Loffhagen D, Reuter S and Weltmann K-D 2015 Stability and excitation dynamics of an argon micro-scaled atmospheric pressure plasma jet *Plasma Sources Sci. Technol.* **24** 065018

[17] Wang S, Schulz-von der Gathen V and Döbele H F 2003 Discharge comparison of nonequilibrium atmospheric pressure Ar/O_2 and He/O_2 plasma jets *Appl. Phys. Lett.* **83** 3272–4

[18] Meek John M and Craggs J D 1982 *Electrical breakdown of gases* (Chichester: Wiley)

[19] Brown S C 1956 Gasentladungen II *Handbuch der Physik* (*Handbuch der Physik/hrsg. von S. Flügge*) ed S Flügge (Berlin and Göttingen and Heidelberg: Springer)

[20] Moravej M, Yang X, Nowling G R, Chang J P, Hicks R F and Babayan S E 2004 Physics of high-pressure helium and argon radio-frequency plasmas *J. Appl. Phys.* **96** 7011

[21] Lieberman M A and Lichtenberg A J 2005 *Principles of Plasma Discharges and Materials Processing* 2nd edn (Hoboken, N. J.: Wiley-Interscience)

[22] Bibinov N, Knake N, Bahre H, Awakowicz P and Schulz-von der Gathen V 2011 Spectroscopic characterization of an atmospheric pressure μ-jet plasma source *J. Phys. D: Appl. Phys.* **44** 345204

[23] Jonkers J, van van de Sande M, Sola A, Gamero A and van der Mullen J 2003 On the differences between ionizing helium and argon plasmas at atmospheric pressure *Plasma Sources Sci. Technol.* **12** 30–8

[24] Golda J, Kogelheide F, Awakowicz P and Schulz-von der Gathen V 2019 Dissipated electrical power and electron density in an RF atmospheric pressure helium plasma jet *Plasma Sources Sci. Technol.* **28** 095023

[25] Golda J *et al* 2016 Concepts and characteristics of the 'COST Reference Microplasma Jet' *J. Phys. D: Appl. Phys.* **49** 084003

[26] Gans T, Schulz-von der Gathen V, Czarnetzki U and Döbele H F 2002 Observation of fast hydrogen atoms formed by ion bombarding of surfaces *Contrib. Plasma Phys.* **42** 596–602

[27] Gans T, Schulz-von der Gathen V and Döbele H F 2004 Prospects of phase resolved optical emission spectroscopy as a powerful diagnostic tool for RF-Discharges *Contrib. Plasma Phys.* **44** 523–8

[28] Schulze J, Gans T, O'Connell D, Czarnetzki U, Ellingboe A R and Turner M M 2007 Space and phase resolved plasma parameters in an industrial dual-frequency capacitively coupled radio-frequency discharge *J. Phys. D: Appl. Phys.* **40** 7008–70

[29] Bischoff L, Hübner G, Korolov I, Donkó Z, Hartmann P, Gans T, Held J, Schulz-von der Gathen V, Liu Y, Mussenbrock T and Schulze J 2018 Experimental and computational investigations of electron dynamics in micro atmospheric pressure radio-frequency plasma jets operated in He/N_2 mixtures *Plasma Sources Sci. Technol.* **27** 125009

[30] McKay K, Iza F and Kong M G 2010 Excitation frequency effects on atmospheric-pressure helium RF microplasmas: plasma density, electron energy and plasma impedance *Eur. Phys. J.* D **60** 497–503

[31] Raizer Y P 1991 *Gas Discharge Physics* (Berlin and New York: Springer)

[32] Schäfer J, Foest R, Reuter S, Kewitz T, Šperka J and Weltmann K-D 2012 Laser schlieren deflectometry for temperature analysis of filamentary non-thermal atmospheric pressure plasma *The Review of Scientific Instruments* **83** 103506

[33] Schäfer J, Bonaventura Z and Foest R 2015 On the fundamental relation of laser schlieren deflectometry for temperature measurements in filamentary plasmas *Eur. Phys. J. Appl. Phys.* **71** 208

[34] Kelly S, Golda J, Turner M M and Schulz-von der Gathen V 2015 Gas and heat dynamics of a micro-scaled atmospheric pressure plasma reference jet *J. Phys. D: Appl. Phys.* **48** 444002

[35] Drawin H W and Emard F 1971 Collisional-radiative volume recombination and ionization coefficients for quasi-stationary helium plasmas *Z. Phys.* A **243** 326–40

[36] Benoy D A, van der Mullen J A M, Van Der Sijde B and Schram D C 1991 A novel collisional radiative model with a numerical bottom and an analytical top *J. Quant. Spectrosc. Radiat. Transfer* **46** 195–210

[37] Bruggeman P J, Iza F and Brandenburg R 2017 Foundations of atmospheric pressure non-equilibrium plasmas *Plasma Sources Sci. Technol.* **26** 123002

[38] O'Neill C, Waskoenig J and Gans T 2012 Tailoring electron energy distribution functions through energy confinement in dual radio-frequency driven atmospheric pressure plasmas *Appl. Phys. Lett.* **101** 154107

[39] Yamabe C, Buckman S J and Phelps A V 1983 Measurement of free-free emission from low-energy-electron collisions with Ar: *Phys. Rev.* A **27** 1345–52

[40] Hofmann S, van Gessel A F H, Verreycken T and Bruggeman P 2011 Power dissipation, gas temperatures and electron densities of cold atmospheric pressure helium and argon RF plasma jets *Plasma Sources Sci. Technol.* **20** 065010

[41] Park J, Henins I, Herrmann H W, Selwyn G S and Hicks R F 2001 Discharge phenomena of an atmospheric pressure radio-frequency capacitive plasma source *J. Appl. Phys.* **89** 20–8

[42] Lazzaroni C, Lieberman M A, Lichtenberg A J and Chabert P 2012 Comparison of a hybrid model to a global model of atmospheric pressure radio-frequency capacitive discharges *J. Phys. D: Appl. Phys.* **45** 495204

[43] Waskoenig J 2010 Numerical simulations of the electron dynamics in single and dual radio-frequency driven atmospheric pressure plasmas and associated plasma chemistry in electro-negative He-O_2 mixtures *PhD Thesis* Queen's University Belfast, Belfast

[44] Hemke T, Eremin D, Mussenbrock T, Derzsi A, Donkó Z, Dittmann K, Meichsner J and Schulze J 2013 Ionization by bulk heating of electrons in capacitive radio frequency atmospheric pressure microplasmas *Plasma Sources Sci. Technol.* **22** 015012

[45] Liu D W, Iza F and Kong M G 2008 Electron heating in radio-frequency capacitively coupled atmospheric-pressure plasmas *Appl. Phys. Lett.* **93** 261503

[46] Schaper L, Waskoenig J, Kong M G, Schulz-von der Gathen V and Gans T 2011 Electron dynamics in a radio-frequency-driven microatmospheric pressure plasma jet *IEEE Trans. Plasma Sci.* **39** 2370–1

[47] Czarnetzki U, Luggenhölscher D and Döbele H F 1999 Space and time resolved electric field measurements in helium and hydrogen RF-discharges *Plasma Sources Sci. Technol.* **8** 230–48

[48] Abroyan I A, Eremeev M A and Petrov N N 1967 Excitation of electrons in solids by relatively slow atomic particles *Sov. Phys. Usp.* **10** 332–67

[49] Hagstrum D H 1954 Auger ejection of electrons from tungsten by noble gas ions *Phys. Rev.* **96** 325–35

[50] Hagstrum D H 1954 Theory of auger ejection of electrons from metals by ions *Phys. Rev.* **96** 336–65

[51] Haynes W M, Lide D R and Bruno T J 2015 *CRC Handbook of Chemistry and Physics: A Ready-Reference Book of Chemical and Physical Data* 96th edn (Boca Raton, FL: Taylor & Francis)

[52] Gellert B and Kogelschatz U 1991 Generation of excimer emission in dielectric barrier discharges *Appl. Phys.* B **52** 14–21

[53] Golda J, Biskup B, Layes V, Winzer T and Benedikt J 2019 Vacuum ultraviolet spectroscopy of cold atmospheric pressure plasma jets *Plasma Process. Polym* e1900216

[54] Andrew R *et al* 2020 Disrupting the spatio-temporal symmetry of the electron dynamics in atmospheric pressure plasmas by voltage waveform tailoring *Plasma Sources Sci. Technol.* **28** 01LT01